



MOX-Report No. 39/2023

**Flattened and wrinkled encapsulated droplets: Shape-morphing
induced by gravity and evaporation**

Riccobelli, D.; Al-Terke, H. H.; Laaksonen, P.; Metrangolo, P.; Paananen, A.;
Ras, R. H. A.; Ciarletta, P.; Vella, D.

MOX, Dipartimento di Matematica
Politecnico di Milano, Via Bonardi 9 - 20133 Milano (Italy)

mox-dmat@polimi.it

<https://mox.polimi.it>

Flattened and wrinkled encapsulated droplets: Shape-morphing induced by gravity and evaporation

Davide Riccobelli,^{1,*} Hedar H. Al-Terke,^{2,3,*} Päivi Laaksonen,⁴ Pierangelo Metrangolo,^{5,2,3}
Arja Paananen,⁶ Robin H. A. Ras,^{2,3} Pasquale Ciarletta,¹ and Dominic Vella^{7,†}

¹*MOX – Dipartimento di Matematica, Politecnico di Milano, Italy*

²*Department of Applied Physics, Aalto University School of Science, Finland*

³*Center of Excellence in Life-Inspired Hybrid Materials (LIBER), Aalto University, Finland*

⁴*HAMK Tech, Häme University of Applied Sciences*

⁵*Department of Chemistry, Materials, and Chemical Engineering “Giulio Natta”, Politecnico di Milano, Italy*

⁶*VTT Technical Research Centre of Finland Ltd, Finland*

⁷*Mathematical Institute, University of Oxford, Woodstock Rd, Oxford, OX2 6GG, UK.*

(Dated: April 8, 2023)

We report surprising morphological changes of suspension droplets (containing class II hydrophobin protein HFBI from *Trichoderma reesei* in water) as they evaporate with a contact line pinned on a rigid solid substrate. Both pendant and sessile droplets display the formation of an encapsulating elastic film as the bulk concentration of solute reaches a critical value during evaporation, but the morphology of the droplet varies significantly: for sessile droplets, the elastic film ultimately crumples in a nearly flattened area close to the apex while in pendant droplets, circumferential wrinkling occurs close to the contact line. These different morphologies are understood through a gravito-elasto-capillary model that predicts the droplet morphology and the onset of shape changes, as well as showing that the influence of the direction of gravity remains crucial even for very small droplets (where the effect of gravity can normally be neglected). The results pave the way to control droplet shape in several engineering and biomedical applications.

The shape of a liquid drop resting on a rigid solid surface is governed by a balance between capillary forces and hydrostatic pressure. For small water droplets, capillarity dominates this balance and the droplet adopts the shape of a spherical cap — a label its shape retains even if it subsequently evaporates, albeit with changing contact angle or radius [1]. While larger water drops may be influenced by gravity, and hence start with more exotic shapes, upon evaporation they must ultimately reach the small droplet limit, and hence adopt the spherical cap shape too. This simple picture of droplets always evaporating as spherical caps does not, however, hold for the evaporation of more complex droplets such as mixtures of water and solid particles or emulsions. In particular, the evaporation of such drops may lead to non-spherical shapes [2–5], reflecting the non-trivial behavior of interfaces including solid-like films formed on the surface from the aggregation of contaminants [3–8]. In these settings and others [9–12] the non-trivial changes in shape that occur are controlled by various balances between surface tension and elasticity and are not generally sensitive to body forces such as gravity.

At the same time, the creation of a capsule around a droplet is useful to protect the inner material from the external environment and, possibly, to selectively release the droplet’s contents under specific conditions [13]. Encapsulation is achieved using a variety of methods [14], including *in-situ* polymerization [15], self-assembly of the capsule [16], elasto-capillary interactions [17], spray drying [18], and gravity-induced encapsulation [19].

Perhaps the simplest method of capsule formation in-

volves a surface-active molecule spontaneously adsorbing at an interface. Here, the properties of the capsule depend on the interfacial concentration of molecules: at low concentrations the interface has a simple interfacial tension but at higher concentrations also develops a solid-like shear modulus [20]. In this Letter, we show that the combination of concentration-dependence and external fields (specifically gravity) gives rise to morphological changes in hydrophobin–water droplets, on a solid substrate, as the water phase evaporates. Specifically, we use class II hydrophobin protein HFBI from *Trichoderma reesei*. HFBI is a water soluble protein and yet is very amphiphilic, readily assembling at air–water or oil–water interfaces [21]. As shown in FIG. 1(C), a sessile droplet (supported against gravity by the surface) starts off as a cap-shape but ultimately forms a flat region close to its apex. Conversely, a pendant droplet (which hangs beneath the surface under gravity) forms wrinkles close to the contact line. While the edge-wrinkling of pendant drops has been modelled previously as an elasto-capillary instability [22], the formation of a central flat spot in the sessile case is still debated: it has previously been proposed that the buoyancy of HFBI molecules drives them to form a raft that then floats to the top (sessile case) or sinks to the edge (pendant case) and forces the interface to be flat in these regions [7, 8]. While these experimental observations (and others on a slope in which the normal to the flat region is parallel to the direction of gravity) strongly suggest that gravity plays a key role in the phenomenon, it stretches credulity that individual molecules (albeit large ones) are affected by gravity to this extent

— a simple calculation shows [23] that the sedimentation length [24] for these molecules $\ell_s \approx 200$ m. Given this gravitational height is so much larger than any length scale in the experiment, we seek to understand how gravity enters the problem, focusing on the role played by its effect on droplet shape. We begin by outlining our own experimental procedures.

Water droplets, with initial volume V_i in the range $8.63 - 18.68 \text{ mm}^3$, containing HFBI molecules were placed on Parafilm substrate; the experimental setup is sketched in FIG. 1(A). The initial concentration C of the HFBI molecules is kept in the range $2 \mu\text{mol L}^{-1} \leq C \leq 4 \mu\text{mol L}^{-1}$. The droplets are monitored using an optical tensiometer and their profile captured using a CCD camera; experimental images are processed using ImageJ and the library openCV [23]. Sessile droplets are found to develop a flattened region during evaporation that is made by a crumpled HFBI monolayer, as shown in FIG. 1(C, D). Pendant droplets are obtained by quickly inverting the substrate after droplet deposition; during evaporation they display a circumferential wrinkling in the vicinity of the contact line, see FIG. 1(C, D).

The crumpling of the flattened region indicates that the elastic film is not flat in its relaxed state and exhibits a non-zero Gaussian curvature. (Similar crumpling has been observed previously in polydopamine-stabilized droplets deflated by syringe suction [3], in polypyrrole droplets[5], as well as in water drops partially covered by a flat polystyrene sheet [25].) Moreover, the formation of wrinkles in pendant droplets suggests that the HFBI film is also present on the entire free surface of the droplets. Therefore, a key first question is to identify the critical threshold for the onset of encapsulation of HFBI droplets.

Analysing the experimental images, we find that the critical volume V_f at which the flattening of sessile droplets is first observed is linearly proportional to the initial amount of HFBI contained in the droplet CV_i (with C the initial concentration and V_i initial volume), see FIG. 2, top. Assuming that flattening starts soon after the encapsulation of droplets, the plot of FIG. 2 suggests that the encapsulation takes place when the bulk concentration of HFBI reaches a given threshold, such that the interfacial concentration (assumed in equilibrium with the bulk) reaches a critical value. Thus, we adopt the following phenomenological law for computing the volume V_e at which the droplet is encapsulated:

$$V_e = \frac{CV_i}{C_e}. \quad (1)$$

where C_e is a constant representing the critical bulk concentration at which the encapsulating membrane is formed. Moreover, in FIG. 2 (bottom) we show the diameter d of the flattened region in sessile droplets as a function of the evaporated volume. Interestingly, the experimental curves display a universal scaling law, since all dimensionless data collapse onto a master curve taking

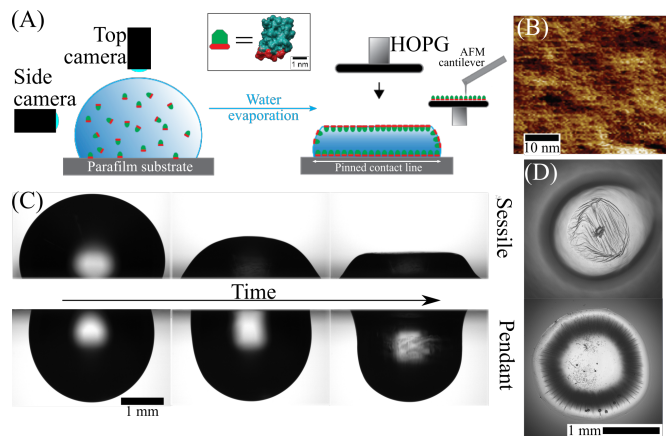


FIG. 1. (A): Sketch of the experimental setup. A droplet is placed on a Parafilm substrate and its shape is recorded from above and the side by cameras. After the formation of the flattened region, a highly ordered pyrolytic graphite (HOPG) substrate was brought in contact with the top of the droplet to perform imaging through an atomic force microscopy (AFM). (B): AFM image of HFBI monolayer at the air-water surface. (C): Sessile (top) and pendant (bottom) droplet shapes at different times during evaporation. The initial volume is $V_i = 13.1 \text{ mm}^3$ in both cases, while the initial concentration of HFBI $2 \mu\text{mol L}^{-1}$ for the sessile drop and $4 \mu\text{mol L}^{-1}$ for the pendant drop. (D): Plan views of a crumpled sessile (left) and a wrinkled pendant (right) droplet.

a length scale $V_i^{1/3}$, suggesting a universal geometrical scaling independent of gravity [23].

We now introduce a theoretical model to unravel the key mechanisms of the observed droplet morphology before and after the formation the elastic film. We distinguish two main phases during the evaporation process. Before the formation of the elastic film, the shape of the drop is dominated by the interplay between gravity and capillarity. We assume axisymmetry and we fix the center of a Cartesian frame (x, y, z) at the apex of the drop. Let $(r(t, S), z(t, S))$ be the curve describing the shape of the droplet at time t , where r is the radial distance from the z axis and S is the arc-length of the curve.

In our experiments we use droplets of characteristic length $V_i^{1/3}$ on the order of millimeters. The Bond number of the droplet (whose sign is positive or negative for sessile or pendant droplets, respectively) $\text{Bo} = \pm \rho g V_i^{2/3} / \gamma$, is therefore $O(1)$ in all the experiments. Hence, gravitational forces are of the same order as capillary forces. The adsorption of HFBI molecules at the interface leads them to self-assemble to form a highly-ordered protein film, with a stretching modulus of similar order to the surface tension [22, 26].

Because of gravity, the pressure inside the drop is $p = p_T - \rho g z$ where p_T is the pressure at $z = 0$. Thus, before the elastic membrane forms, the droplet shape is

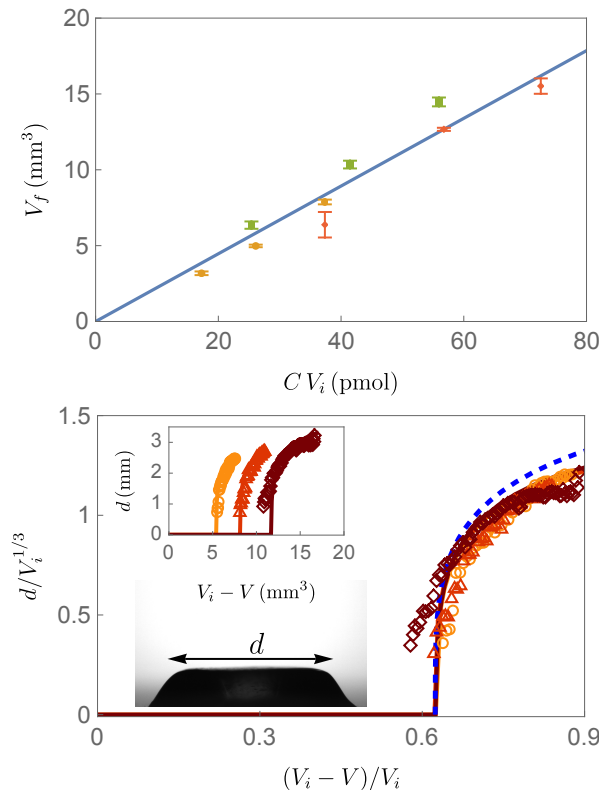


FIG. 2. (Top): Experimental data for the droplet volume V_f at which the sessile droplets start to flatten as a function of the total number of HFBI molecules contained in the droplet (the product of initial concentration C and initial droplet volume V_i). The orange, green and red dots represent the data for $C = 2, 3, 4 \mu\text{mol L}^{-1}$, respectively. The blue solid line shows the linear fit of the experimental data. (Bottom): The diameter, d , of the flat spot increases with the volume of liquid lost to evaporation, $V_i - V$. Raw measurements for droplets with $C = 2 \mu\text{mol L}^{-1}$ and $V_i = 8.63, 13.05, 18.68 \text{ mm}^3$ (yellow, red, and brown, respectively) shown in the inset collapse onto a master curve when lengths are rescaled by $V_i^{1/3}$. The blue dashed curve shows the prediction of a purely geometrical model, see Eq. (S22) of [23].

governed by the Young–Laplace equation at the interface

$$\rho g z - p_T = \gamma \kappa. \quad (2)$$

where γ is the surface tension and κ is twice the mean curvature. If ϕ denotes the angle between the tangent and the radial direction, $\kappa = \pm (d\phi/dS + \sin \phi/r)$, where the sign is positive or negative for sessile or a pendant droplets, respectively. Using as initial conditions $r(t, 0) = z(t, 0) = 0$, we numerically solve the Young–Laplace equation (2) for a fixed value of p_T in the interval $S \in (0, S_{\text{end}})$ with $r(t, S_{\text{end}})$ equal to the fixed contact radius r_c [23].

Once the bulk HFBI concentration reaches the critical value C_e , i.e. the droplet reaches the critical volume V_e given by equation (1), HFBI molecules at the free surface self-organize into a monolayer with a hexagonal

structure, as shown in FIG. 1 (B). In this second phase, the shape of the droplet is dictated by the interplay between the film elasticity and the gravitational forces on the droplet. Since the bending modulus B of the HFBI film is proportional to the cube of the membrane thickness (proportional to the size of a HFBI droplet), the bendability $\gamma V_i^{2/3}/B$ is much larger than 1 and the elastic film can be modeled as an elastic membrane [27].

Denoting by r_0 and z_0 the radial and axial coordinates, respectively, of the membrane cross-section as the HFBI film forms, let $s_0 \in [0, L]$ be the arc-length of this initial curve. Its current configuration during evaporation, is described by the current coordinates r and z , with the interface parametrized by the arc-length $s = s(s_0)$.

Taking account of both elastic and capillary forces, the membrane assumption for the meridional and hoop stresses τ_s and τ_θ gives

$$\begin{cases} \tau_s = \frac{E}{1-\nu^2} \frac{1}{\lambda_\theta} [(\lambda_s - 1) + \nu(\lambda_\theta - 1)] + \gamma, \\ \tau_\theta = \frac{E}{1-\nu^2} \frac{1}{\lambda_s} [(\lambda_\theta - 1) + \nu(\lambda_s - 1)] + \gamma, \end{cases} \quad (3)$$

where E is the 2D Young’s modulus, ν is the 2D Poisson’s ratio, while $\lambda_s = ds/ds_0$ and $\lambda_\theta = r/r_0$ are the meridional and hoop stretches, respectively [28]. We remark that the elastic membrane is in tension at the instant of film formation (when $\lambda_s = \lambda_\theta = 1$) thanks to capillary forces.

Assuming quasi-static deformations, the following force balance equations must be imposed:

$$\begin{cases} \frac{d}{ds}(r\tau_s) - \tau_\theta \cos \phi = 0, \\ \kappa_s \tau_s + \kappa_\theta \tau_\theta = \rho g z - p_T \end{cases} \quad (4)$$

where κ_s and κ_θ are the principal curvatures along the meridional and hoop directions, respectively. In (4), the first equation represents in-plane equilibrium, while the latter represents equilibrium normal to the interface and hence is the elastic counterpart of the Young–Laplace equation (2). Setting the boundary conditions $r(0) = \phi(0) = 0$, the ordinary differential system is numerically solved by fixing the value of $\tau_s(0)$ and by performing a shooting method with the parameter p_T until the boundary condition $r(t, L) = r_c$ is satisfied [23].

As water evaporates, surface tension is counteracted by compressive elastic stresses within the membrane, depending on the dimensionless elastocapillary ratio E/γ . Since the film has negligible bending stiffness, it buckles immediately upon compression forming wrinkles (if the compression is uniaxial) or crumples (if the compression is biaxial). To understand the shape evolution beyond the onset of crumpling/wrinkling, we apply a far-from-threshold analysis [22, 27], assuming that the membrane undulations have small amplitude and short wavelength.

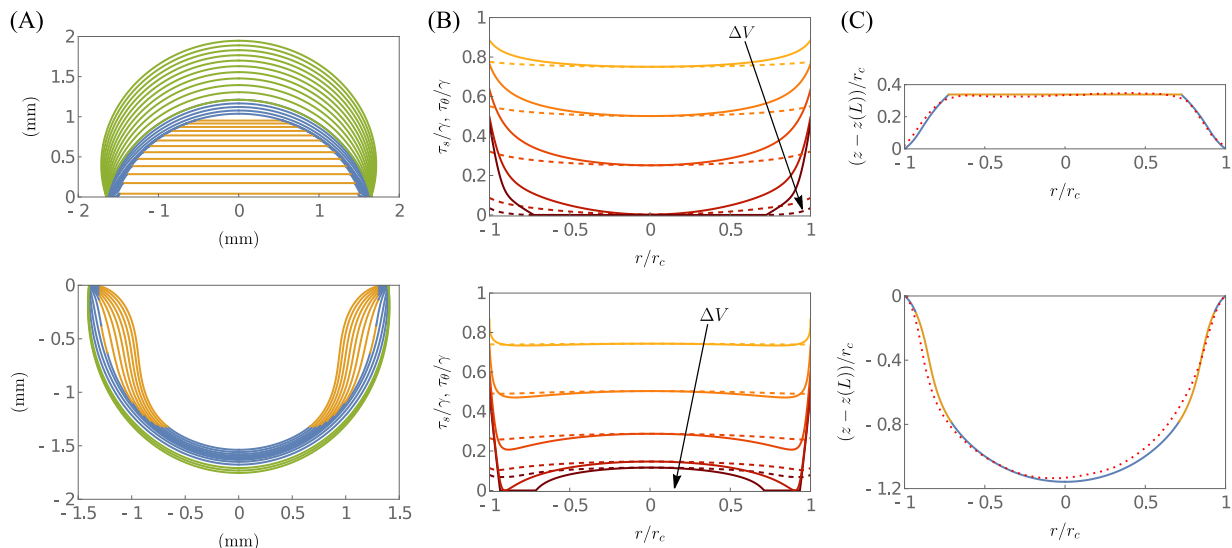


FIG. 3. (A): Theoretical predictions of the droplet profiles during evaporation of a sessile (top, $V_i = 13.05 \text{ mm}^3$, $C = 2 \mu\text{mol L}^{-1}$, $\text{Bo} = 0.99$) and a pendant droplet (bottom, $V_i = 7.77 \text{ mm}^3$, $C = 4 \mu\text{mol L}^{-1}$, $\text{Bo} = -0.70$). The green solid curves are obtained from the fluid equation (2), which remains valid while the bulk concentration $C < C_e$; while for $C \geq C_e$ the elastic equations (3), (4) are solved. Blue and orange solid curves indicate the elastic regions and wrinkled/crumpled regions of the interface, respectively. (B): Dimensionless meridional (dashed curves) and hoop stress (solid curves) versus the dimensionless radial position r/r_c at different volumes V ($V = 3.57, 4.91, 5.26, 5.60, 5.93 \text{ mm}^3$ for the sessile droplet, while $V = 5.77, 6.15, 6.43, 6.76, 7.10 \text{ mm}^3$ for the pendant droplet), the arrows indicate the direction of increasing evaporated volume ΔV . (C): Predicted (solid curves) and experimental droplet profiles (dotted curves) at a given time for a sessile (top, $V = 3.57 \text{ mm}^3$) and a pendant droplet (bottom, $V = 5.77 \text{ mm}^3$). Here color shows the predicted wrinkled/crumpled (yellow) or tensile (blue) regions.

In particular, we describe the elastic film through an axisymmetric pseudosurface $(r(t, s_0), z(t, s_0))$ around the buckled (non-axisymmetric) mid-surface.

For sessile droplets, our theory predicts that the apex of the membrane becomes crumpled during evaporation. We assume that the stress is completely released therein, i.e. $\tau_s = \tau_\theta = 0$ in a portion of the membrane $s_0 \in [0, s_f]$; since both τ_s and τ_θ vanish in this region, the HFBI film cannot sustain a pressure difference across it, and so we must have $p_T = 0$ and the interface is flat. Hence, a flat spot appears at the apex of the droplet, as observed experimentally. Beyond the flat spot, (4) continues to hold. It is possible to show that the actual radius of the flattened region is given by $r(t, s_f) = E/(E + \gamma - \gamma\nu)r_0(t, s_f)$ [23]. Using this boundary condition, we numerically integrate the system (4) for $s_0 \in [s_f, L]$ by fixing s_f and using a shooting method to find the value of $\phi(t, s_f)$ at which the boundary condition $r(t, L) = r_c$ is satisfied. The resulting diameter of the crumpled region collapses on a master curve when plotted versus the evaporated volume, in excellent agreement with the experimental findings (see FIG 2, bottom). This collapse can be explained using a geometrical argument that explicits the closeness of the droplet shape to a spherical cap [23]. A similar numerical scheme is applied to model pendant droplets [22]; here we find that only the hoop stress vanishes in a region $[s_a, s_b] \subseteq [0, L]$; radial wrinkles therefore form and the balance equations (4) are modified by set-

ting $\tau_\theta = 0$ for $s_0 \in [s_a, s_b]$ [23].

In the numerical simulations, we set $E = 400 \text{ mN m}^{-1}$, $\nu = 0.5$, $\gamma = 55 \text{ mN m}^{-1}$, and $C_e = 4.17 \mu\text{mol L}^{-1}$. The numerical results display excellent agreement with experimentally-determined profiles for both sessile and pendant droplets. Two illustrative examples of the morphological evolution of the pendant and the sessile droplets during evaporation are shown in FIG. 3. We remark that, despite the morphological differences between the pendant and the sessile droplets, in both the cases the hoop stress exhibits huge variations along the radial direction and is maximal near the contact line (namely for s_0 close to L), while the meridional stress is nearly constant. Specifically, at the apex the stress is a locally convex or concave function of the radial coordinate if the droplet is sessile or pendant, respectively, see FIG. 3. This stress distribution is key to whether crumples or wrinkles form: for both sessile and pendant drops, the stress is isotropic close to the apex, i.e. $\tau_s \approx \tau_\theta$. For sessile droplets this isotropic stress is a global minimum so that both stresses become compressive simultaneously, leading to crumpling at the apex. For pendant droplets both stresses are locally maximal at the apex, with a global minimum in τ_θ close to the contact line — compression occurs with $\tau_\theta = 0$, $\tau_s > 0$ and wrinkles appear.

Figure 4 shows a morphological diagram for evaporating HFBI-water droplets in terms of the dimensionless parameters Bo and E/γ . This plot emphasizes the un-

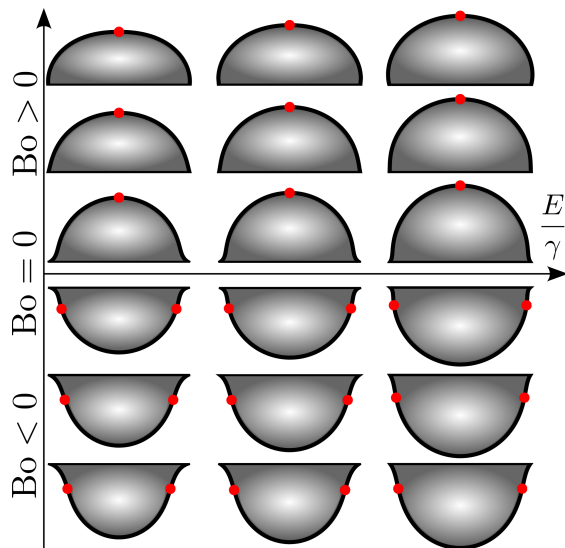


FIG. 4. Morphological diagram of the droplets with respect to the dimensionless parameters Bo and E/γ at the onset of wrinkling ($Bo < 0$) and crumpling ($Bo > 0$). Red dots indicate the nucleation points of wrinkling/crumpling. We set $Bo = \pm 0.07, \pm 0.7, \pm 1.4$, with constant initial volume, and $E/\gamma = 2.7, 3.6, 7.3$.

usual change in behavior seen as Bo changes sign: the two drop shapes with $Bo = \pm 0.07$ and fixed E/γ are very similar (as should be expected for small $|Bo|$). Nevertheless, the location at which wrinkles/crumples are nucleated is very different in the two cases. FIG. 4 also shows that at fixed drop volume (fixed Bo) a smaller volume decrease is required to induce compression as the dimensionless elasticity, E/γ , increases.

In this Letter we have presented a theoretical framework to predict the morphological changes observed during the evaporation of sessile and pendant HFBI-water droplets. Our experiments show that the HFBI molecules self-assemble creating an encapsulating monolayer when the bulk concentration of HFBI molecules reaches a critical value, C_e . Upon further evaporation, the stress in this layer becomes compressive and the layer wrinkles or crumples. Surprisingly, these changes strongly depend on the direction of gravity, with a discontinuous transition between a flat spot at the apex, and wrinkles near the contact line as Bo changes sign. This distinction is observed experimentally and quantitatively explained by our gravito-elasto-capillary model. The droplet morphology results from the interplay between elasticity, capillarity, evaporation, and gravity, as summarized in FIG. 4. This new understanding may be used to propose effective mechanisms to encapsulate droplets that change their shape on demand. Controlling the morphological changes that take place as the volume of the encapsulated droplet decreases (through either evaporation or the controlled release or removal of the encapsulate [29]) has many applications. For example, change of shape can be used

to target adhesion on surfaces [30], to regulate drag in fluid-structure interaction [31], or to control depinning of heated droplets in microgravity conditions [32]. Future efforts will be devoted to the study of picoliter HFBI droplets, as well as droplets resting on a nonrigid substrate (e.g. elastic or liquid substrates).

This work has been partially supported by MUR (PRIN grant MATH4I4 2020F3NCPX), by Regione Lombardia (NEWMED grant, ID: 117599, POR FESR 2014-2020), by GNFM – INdAM, by the Academy of Finland (Center of Excellence Program (2022-2029) in Life-Inspired Hybrid Materials (LIBER) project number 346109). We also acknowledge the provision of facilities and technical support by Aalto University at the OtaNano Nanomicroscopy Center.

* These two authors contributed equally.

† dominic.vella@maths.ox.ac.uk

- [1] P.-G. de Gennes, F. Brochard-Wyart, and D. Quéré, *Capillarity and wetting phenomena: drops, bubbles, pearls, waves*, Vol. 315 (Springer, 2004).
- [2] A. B. Subramaniam, M. Abkarian, L. Mahadevan, and H. A. Stone, *Nature* **438**, 930 (2005).
- [3] H. Abe, T. Matsue, and H. Yabu, *Langmuir* **33**, 6404 (2017).
- [4] G. Kaufman, W. Liu, D. M. Williams, Y. Choo, M. Gopinadhan, N. Samudrala, R. Sarfati, E. C. Y. Yan, L. Regan, and C. O. Osuji, *Langmuir* **33**, 13590 (2017).
- [5] H. Kim, K. Kim, and S. J. Lee, *Macromol. Mater. Eng.* **304**, 1970006 (2019).
- [6] A. B. Subramaniam, M. Abkarian, and H. A. Stone, *Nat. Mater.* **4**, 553 (2005).
- [7] R. Yamasaki, Y. Takatsuji, H. Asakawa, T. Fukuma, and T. Haruyama, *ACS Nano* **10**, 81 (2016).
- [8] R. Yamasaki and T. Haruyama, *J. Phys. Chem. B* **120**, 3699 (2016).
- [9] N. Denkov, S. Tcholakova, I. Lesov, D. Cholakova, and S. K. Smoukov, *Nature* **528**, 392 (2015).
- [10] P. A. Haas, R. E. Goldstein, S. K. Smoukov, D. Cholakova, and N. Denkov, *Phys. Rev. Lett.* **118**, 088001 (2017).
- [11] I. García-Aguilar, P. Fonda, E. Sloutskin, and L. Giomi, *Phys. Rev. Lett.* **126**, 038001 (2021).
- [12] K. Peddireddy, S. Čopar, K. V. Le, I. Mušević, C. Bahr, and V. S. R. Jampani, *Proc. Natl Acad. Sci. USA* **118**, e2011174118 (2021).
- [13] A. D. Dinsmore, M. F. Hsu, M. G. Nikolaides, M. Marquez, A. R. Bausch, and D. A. Weitz, *Science* **298**, 1006 (2002).
- [14] M. G. Bah, H. M. Bilal, and J. Wang, *Soft Matter* **16**, 570 (2020).
- [15] E. N. Brown, M. R. Kessler, N. R. Sottos, and S. R. White, *J. Microencapsul.* **20**, 719 (2003).
- [16] C. J. Brinker, Y. Lu, A. Sellinger, and H. Fan, *Adv. Mater.* **11**, 579 (1999).
- [17] C. Py, P. Reverdy, L. Doppler, J. Bico, B. Roman, and C. N. Baroud, *Phys. Rev. Lett.* **98**, 156103 (2007).
- [18] M. I. Ré, *Dry. Technol.* **16**, 1195 (1998).

- [19] M. Abkarian, S. Protière, J. M. Aristoff, and H. A. Stone, *Nat. Commun.* **4**, 1895 (2013).
- [20] M. A. Bos and T. van Vliet, *Adv. Colloid Interface Sci.* **91**, 437 (2001).
- [21] H. Hähl, A. Griffo, N. Safaridehkohneh, J. Heppe, S. Backes, M. Lienemann, M. B. Linder, L. Santen, P. Laaksonen, and K. Jacobs, *Langmuir* **35**, 9202 (2019).
- [22] S. Knoche, D. Vella, E. Aumaitre, P. Degen, H. Rehage, P. Cicuta, and J. Kierfeld, *Langmuir* **29**, 12463 (2013).
- [23] Please see the Supplemental Material for details on the experimental setup and the mathematical model.
- [24] R. Piazza, S. Buzzaccaro, and E. Secchi, *J. Phys.: Condens. Matter* **24**, 284109 (2012).
- [25] H. King, R. D. Schroll, B. Davidovitch, and N. Menon, *Proc. Natl. Acad. Sci. U.S.A.* **109**, 9716 (2012).
- [26] H. H. Al-Terke, *Study of hydrophobin behaviour at air-water interface*, Master's thesis, Aalto University (2017).
- [27] B. Davidovitch, R. D. Schroll, D. Vella, M. Adda-Bedia, and E. A. Cerda, *Proc. Natl. Acad. Sci. U.S.A.* **108**, 18227 (2011).
- [28] A. Libai and J. G. Simmonds, *The Nonlinear Theory of Elastic Shells* (Cambridge University Press, 1998).
- [29] G. Ma, *J. Control. Release* **193**, 324 (2014).
- [30] P. Decuzzi, R. Pasqualini, W. Arap, and M. Ferrari, *Pharm. Res.* **26**, 235 (2008).
- [31] D. Terwagne, M. Brojan, and P. M. Reis, *Adv. Mater.* **26**, 6608 (2014).
- [32] S. Kumar, M. Medale, P. Di Marco, and D. Brutin, *npj Microgravity* **6**, 37 (2020).

MOX Technical Reports, last issues

Dipartimento di Matematica
Politecnico di Milano, Via Bonardi 9 - 20133 Milano (Italy)

- 38/2023** Africa, P. C.; Fumagalli, I.; Bucelli, M.; Zingaro, A.; Dede', L.; Quarteroni, A.
lifex-cfd: an open-source computational fluid dynamics solver for cardiovascular applications
- 37/2023** Regazzoni, F.; Pagani, S.; Salvador, M.; Dede', L.; Quarteroni, A.
Latent Dynamics Networks (LDNets): learning the intrinsic dynamics of spatio-temporal processes
- 34/2023** Caldana, M.; Antonietti, P. F.; Dede', L.
A Deep Learning algorithm to accelerate Algebraic Multigrid methods in Finite Element solvers of 3D elliptic PDEs
- 35/2023** Ferrari, L.; Manzi, G.; Micheletti, A.; Nicolussi, F.; Salini, S.
Pandemic Data Quality Modelling: A Bayesian Approach
- 32/2023** Gambarini, M.; Ciaramella, G.; Miglio, E.; Vanzan, T.
Robust optimization of control parameters for WEC arrays using stochastic methods
- 31/2023** Orlando, G.
Assessing ChatGPT for coding finite element methods
- 30/2023** Antonietti, P. F.; Bonizzoni, F.; Verani, M.
A DG-VEM method for the dissipative wave equation
- 29/2023** Carbonaro, D.; Mezzadri, F.; Ferro, N.; De Nisco, G.; Audenino, A.L.; Gallo, D.; Chiastra, C.; Morbiducci, U.; Perotto, S.
Design of innovative self-expandable femoral stents using inverse homogenization topology optimization
- 28/2023** Zingaro, A.; Vergara, C.; Dede', L.; Regazzoni, F.; Quarteroni, A.
A comprehensive mathematical model for myocardial perfusion
- Fumagalli, A.; Panzeri, L.; Formaggia, L.; Scotti, A.; Arosio, D.
A mixed-dimensional model for direct current simulations in presence of a thin high-resistivity liner